Development and Initial Testing of a Magnetically Shielded Miniature Hall Thruster

Ryan W. Conversano, Dan M. Goebel, *Fellow, IEEE*, Richard R. Hofer, Taylor S. Matlock, and Richard E. Wirz

***Abstract*— The scaling of magnetically shielded Hall thrusters to low power is investigated through the development and fabrication of a 4-cm Hall thruster. During initial testing, the magnetically shielded miniature Hall thruster was operated at 275 V discharge voltage and 325-W discharge power. Inspection of the channel walls after testing suggests that the outer discharge channel wall was successfully shielded from high-energy ion erosion while the inner channel wall showed evidence of weaker shielding, likely due to magnetic circuit saturation. Scanning planar probe measurements taken at two locations downstream of the thruster face provided ion current density profiles. The ion current calculated by integrating these data was 1.04 A with a plume divergence half-angle of 30°. Swept retarding potential analyzer measurements taken 80-cm axially downstream of the thruster measured the most probable ion voltage to be 252 V. The total thruster efficiency was calculated from probe measurements to be 43% (anode efficiency of 59%) corresponding to a thrust of 19 mN at a specific impulse of 1870 s. Discharge channel erosion rates were found to be approximately three orders of magnitude less than unshielded Hall thrusters, suggesting the potential for a significant increase in operational life.**

***Index Terms*— Hall effect devices, magnetic fields.**

I. Introduction

AN EFFICIENT, long-life, low-power Hall thruster would be attractive for a wide range of NASA missions. Such a thruster would provide deep space and near Earth mission planners with the combined advantages of high specific impulse (>1500 s) and high thrust-to-power ratio (>50 mN/kW) at a reduced scale. Numerous miniature Hall thrusters have been developed in an effort to meet this need. The BHT-200, for example, employs a 3-cm discharge channel diameter and generates up to 12.8 mN of thrust at a specific impulse of 1390 s and an anode efficiency of 44% (nominal thruster parameters are 11.4 mN, 1570 s, and 42%); however, the BHT-200's operational life is limited to approximately 1000 h [1]–[5]. The SPT-30, also a 3-cm Hall thruster, produces a thrust of 11.3 mN and a specific impulse of 1170 s at an anode efficiency of 32%, and is limited to approximately 600 h of total operation [6]. The primary challenges for Hall thrusters at small scales (<500 W and <7 cm diameter) are poor life and low efficiency due to rapid erosion of and high electron-losses to the discharge channel walls; these result from the inherently higher surface-to-volume ratio of small thrusters. To combat low performance and efficiency caused by high surface-to-volume ratios, miniature Hall thrusters are often designed with wide discharge channels relative to the size of the thruster. This corresponds to an increased channel volume compared with the channel surface area, thereby reducing the surface-to-volume ratio at reduced scales. The discharge channel width-to-mean-diameter ratio (b/d_m) of several well-known Hall thrusters is plotted in Fig. 1 against their power level, showing an increasing trend of b/d_m as a Hall thruster's scale is reduced [7], [9].

Manuscript received November 25, 2013; revised February 26, 2014 and March 24, 2014; accepted March 25, 2014. This work was supported in part by the University of California at Los Angeles School of Engineering and Applied Sciences, in part by the NASA Space Technology Research Fellowship under Grant NNX13AM65H, and in part by the Jet Propulsion Laboratory, California Institute of Technology, Pasadena, CA, USA, through the National Aeronautics and Space Administration.

R. W. Conversano, T. S. Matlock, and R. E. Wirz are with the Plasma and Space Propulsion Laboratory, Wirz Research Group, University of California at Los Angeles, Los Angeles, CA 90095 USA (e-mail: ryan.w.conversano@jpl.nasa.gov; tmatlock17@ucla.edu; wirz@ucla.edu).

D. M. Goebel and R. R. Hofer are with the Jet Propulsion Laboratory, Electric Propulsion Group, California Institute of Technology, Pasadena, CA 91109 USA (e-mail: dan.m.goebel@jpl.nasa.gov; richard.r.hofer@jpl.nasa.gov).

Color versions of one or more of the figures in this paper are available online at http://ieeexplore.ieee.org.

Digital Object Identifier 10.1109/TPS.2014.2321107

II. Background and Motivation

A. Hall Thruster Life Limiting Factors

The primary life-limiting factor of conventional Hall thrusters is erosion of the discharge channel walls from ion bombardment. Due to the zero net current condition at the insulating walls, a large sheath potential forms to reject the bulk of the electron population. In turn, the electron repelling sheath adds to the radial electric field component from the bulk plasma that accelerate nearby ions into the walls [10], [11]. The resultant sputter erosion of the wall is concentrated near the exit plane and can wear through the discharge channel walls, exposing the thruster's pole pieces to ion bombardment. Degradation of the pole pieces alters the interior magnetic circuit of the device, eventually degrading the performance of the thruster and ending its useful life [12].

Another key performance-limiting factor in Hall thrusters is high-energy electron power loss to the discharge channel walls. In conventional Hall thrusters, the radial magnetic field lines near the exit plane intersect the channel walls. High-energy electrons flow along these field lines, and the most energetic ones bombard the discharge channel walls while the bulk of the distribution is reflected back into the plasma by either the plasma sheath or the magnetic mirror created at the pole pieces. This electron power deposition results in performance-robbing heating of the Hall thruster that can also

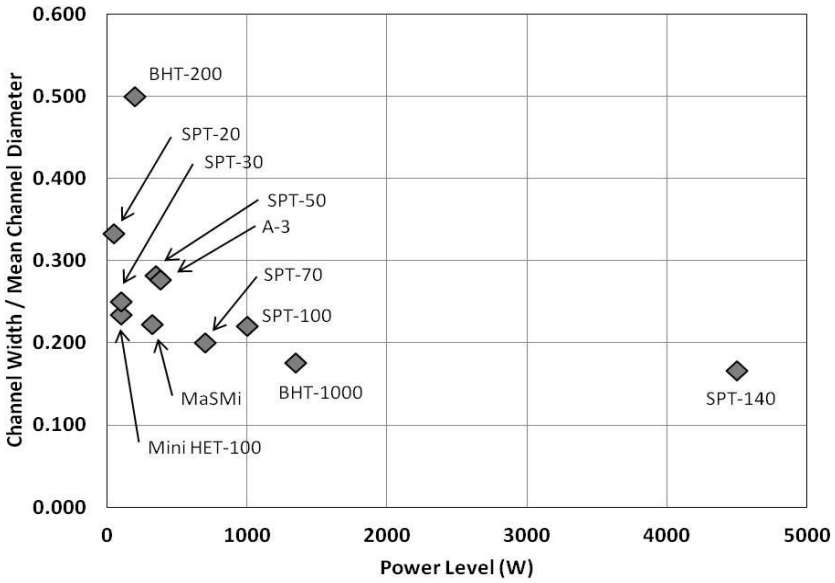

Fig. 1. Trends of discharge channel width-to-mean-diameter ratio as a function of input power for a range of Hall thrusters [3]–[9].

affect operational lifetime due to temperature limitations of the thruster's materials and construction [13], [14].

Ion bombardment and electron power loss effects increase rapidly in low-power Hall thrusters primarily due to their characteristically larger surface-to-volume ratios. The erosion rates of conventionally sized and miniature Hall thrusters are comparable; however, shorter operational lifetimes are observed in miniature devices due to their reduced channel wall thickness. Operational lifetimes of miniature Hall thrusters are generally low, ranging from tens of minutes to hundreds of hours with a few devices surviving beyond 1000 h [5], [6], [15].

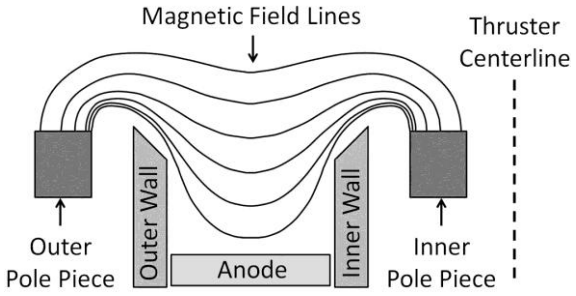

Fig. 2. Illustration of the lines of force in a magnetically shielded Hall thruster.

B. Magnetic Shielding Theory

Magnetic shielding is a method of dramatically increasing the operational life of Hall thrusters by significantly reducing the aforementioned life-limiting factors through careful design of the magnetic circuit. Magnetic shielding was first described by JPL and Aerojet-Rocketdyne after the BPT-4000 reached a zero-erosion state 5600 h into a 10 400 h wear test [16], [17]. Subsequently, magnetic shielding was shown to reduce erosion rates by three orders of magnitude in a series of simulations and experiments specifically designed to more completely understand and describe the physics of magnetic shielding through modification of the H6 Hall thruster (called the H6MS) [10], [11], [18], [19]. Through nearly 5000 h of wear testing in a zero-erosion configuration with the BPT-4000 and detailed simulations and experiments with the H6MS, the physics of magnetic shielding have been established for thrusters operating at 4.5–6 kW and ∼2000 s specific impulse. The extensibility of magnetic shielding to higher specific impulse, high power density, higher power, lower power, and alternate wall materials are key questions now being addressed by NASA as the limits of magnetic shielding are explored [20]–[24].

Magnetically shielded Hall thrusters benefit from a unique magnetic field topology that prevents the magnetic field lines from intersecting the discharge channel walls in the acceleration region. Instead, the lines of force originating from both the inner and outer pole pieces curve around the downstream edges of the discharge channel and follow the channel walls toward the anode, as shown in Fig. 2. This unique field topology results in low electron temperature at the discharge channel walls while eliminating strong electric field components that would otherwise lead to high erosion rates from ion acceleration into the channel walls.

Several well-known properties of Hall thrusters are exploited in a magnetically shielded field topology [25]–[27]. The isothermality of magnetic lines of force assumes that the electron temperature (T_e) along a field line is essentially constant, or $T_e \approx T_{e0}$, where T_{e0} is the reference, or channel centerline, electron temperature. This property allows the deep-penetrating magnetic field lines to capture cold (∼5 eV) electrons near the anode and transport these electrons adjacent to the discharge channel walls, maintaining a low average electron temperature near the wall [10], [11], [17], [28]. Because the sheath potential is a function of electron temperature for a given material, the low electron

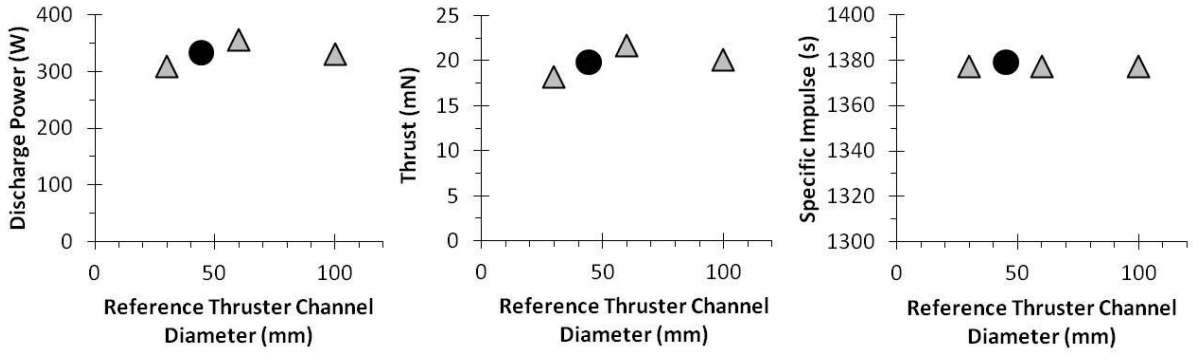

Fig. 3. Predicted discharge power, thrust, and specific impulse for MaSMi based on scaling laws [7], [8]. The triangles represent MaSMi's predicted performance based on each reference thruster (BHT-200, A3, and SPT-100) [4]–[9]; the circles represent MaSMi's predicted performance averaged over the reference thrusters and plotted at its selected outer channel diameter.

temperature yields lower sheath potentials at the discharge channel walls.

Another byproduct of the cold field lines is that the assumption of magnetic-force-line equipotentialization will hold to a greater extent near the walls than in conventional Hall thrusters. This is seen through the thermalized potential equation

$$\Phi \approx \Phi_0 + T_{e0} \times \ln\left(\frac{n_e}{n_{e0}}\right) \tag{1}$$

where Φ is the plasma potential, n_e is the electron density, and the subscript 0 denotes the channel centerline (reference) values. A magnetically shielded Hall thruster therefore maintains a plasma potential close to that of the discharge voltage along the length of the discharge channel [10], [11]. Additionally, proper channel geometry and magnetic field design forces the electric field to point nearly perpendicular to the discharge channel surfaces [10], [11].

In a properly designed magnetically shielded Hall thruster, magnetic field line isothermality and magnetic-force-line equipotentialization significantly reduce the kinetic energy gained by ions passing through the potential drop along the channel walls, thereby decreasing sputter erosion of the channel. The result is an increase of thruster lifetimes by as much as a factor of 1000 compared with unshielded Hall thrusters [10], [11]. Additionally, because the field lines do not intersect with the thruster walls, high-energy electron confinement is improved while power deposition to the walls is reduced. In terms of performance, the implementation of magnetic shielding on the H6 Hall thruster resulted in a slight drop in efficiency (1.7%), a significant drop in insulator ring (discharge channel downstream edge) temperature (12%–16%), and an increase in specific impulse (2.9%) primarily due to an increase in multiply charged ions from the decreased electron wall losses and resulting higher electron temperature [10], [11].

C. Objective

The goal of this investigation is to develop a miniature (∼4-cm diameter) Hall thruster operating in the 300–400 W range that demonstrates significantly increased operational lifetimes and improved performance compared with existing low-power Hall thrusters. We aim to develop a detailed understanding of the physical mechanisms of magnetic shielding as it is applied to miniature Hall thrusters and to determine to what extent magnetically shielding a miniature Hall thruster can result in:

1) significantly increased lifetimes resulting from nearly eliminating wall erosion;
2) improved performance resulting from the reduction of plasma–wall interactions.

The thruster designed, fabricated, and tested for this investigation will herein be called the magnetically shielded miniature (MaSMi) Hall thruster. An analysis of the MaSMi Hall thruster's dimensions and predicted performance is presented in Section III, followed by a discussion of the experimental investigation in Sections IV and V.

III. Thruster Design and Predicted Performance

A. Scaling Method and Results

Hall thrusters present unique design challenges as they are scaled to the sub-7-cm channel diameter regime. As the scale is reduced, the increase in the thruster's surface-to-volume ratio significantly contributes to the nonlinear scaling of miniature Hall thrusters [7], [8]. Additionally, no scaling laws exist yet for magnetically shielded thrusters. As a means to roughly approximate MaSMi's performance, a proven scaling method for conventional Hall thrusters was applied [7], [8]. Using the BHT-200 (30 mm channel outer diameter), the A-3 (60-mm channel outer diameter), and the SPT-100 (100-mm channel outer diameter) as reference thrusters, the performance of a 44 mm (channel outer diameter) thruster was predicted [4]–[9]. The discharge power, thrust, and specific impulse of the 44-mm thruster were calculated based on each reference thruster using the scaling model [7], [8].

The predicted performance values for the 44-mm thruster were plotted against each reference thrusters' respective channel diameter (triangles) and the average performance was plotted against the thruster's designed diameter of 44 mm (circles), as shown in Fig. 3. The nonlinear scaling trends result from the many variables changing in the optimization of each design. The applied scaling laws predict a discharge power of approximately 330 W, a thrust of approximately 20 mN, and a specific impulse of ∼1380 s.

B. Key Dimensions

The MaSMi Hall thruster employs an outer channel diameter of 44 mm and a mean channel diameter of 36 mm. A model of the thruster's magnetic circuit predicts a magnetically shielded field topology with no intersection of the magnetic field lines and the discharge channel walls. Additionally, the predicted maximum magnetic field strength exceeded the required value to constrain electron Larmor radii to 10% of the discharge channel width (assuming an electron temperature of 20 eV) as is generally deemed optimal [14].

Iron is conventionally used for Hall thruster magnetic cores due to its favorable magnetic properties and low cost; however, it displays severe magnetic saturation problems at small thruster scales. Hiperco (an iron-cobalt-vanadium alloy), which has a much higher magnetic saturation tolerance than iron, was therefore selected for MaSMi's magnetic core. A single inner coil and a single outer coil, wrapped from AWG-22 nickel-plated and fiberglass-insulated high temperature copper magnet wire (rated to over 400 °C), provide the necessary fields to operate the thruster.

The discharge channel, machined from HP-grade boron nitride (BN), has an 8-mm channel width and chamfered downstream edges characteristic of magnetically shielded thrusters to avoid intersection with magnetic field lines. The thruster has a channel width-to-mean-diameter ratio of 0.222, placing it in line with the trends of conventional miniature Hall thrusters shown in Fig. 1. According to conventional Hall thruster design theory, the discharge channel length should be no less than three times the ionization length to allow for proper thruster operation [14]. The mean free path for ionization collisions is between 2 and 6 mm based on MaSMi's expected performance range. A maximum discharge channel length of 16 mm (providing a maximum discharge channel length-to-width ratio of 2) was selected to allow for variable anode placement within the channel to optimize propellant mixing and ionization. During initial testing, the full 16-mm discharge channel length was used.

The anode employs a two-chamber design for uniform propellant distribution: the first chamber is intended to choke the propellant flow while the second has an annular diffuser to encourage an even propellant flow distribution into the channel [29]. The dividing plate (between the two chambers) and the downstream diffuser rings face the discharge plasma during operation and are therefore machined from graphite to provide high emissivity and lower operating temperatures. The remaining parts of the anode are machined from stainless steel.

C. Performance Modeling

1) Power Balance: The total power deposition to the discharge channel walls and anode can be estimated based on the thruster's operating parameters. It should be noted that the equations used for this power deposition model apply only to unshielded Hall thrusters; therefore, the power deposition experienced by MaSMi is expected to be significantly less than the model predicts. A linear curve fit of the secondary electron yield of BN is used to predict finite secondary electron yields at low incident energies [30]. The electron temperature at the thruster exit plane is then calculated using an iterative process outlined in the literature based on the linear secondary electron yields and the thruster operating parameters [14]. The power input to the thruster to generate the beam (i.e., the discharge power, P_d), which by definition is equal to the total power out of the thruster, is modeled to the first order as

$$P_d = P_b + P_w + P_a + P_R + P_i \tag{2}$$

where P_b is the beam power, P_w is the power deposited to the discharge channel walls by electrons and ions, P_a is the power deposited to the anode by electrons, P_R is the plasma's radiative power loss, and P_i is the power to produce ions that either become the beam or bombard the channel walls.

These power terms are presented in the literature as

$$P_b = V_b I_b \tag{3}$$

$$P_w = n_e e A_w \left[\left(\frac{kT_e}{e} \right)^{3/2} \left(\frac{2e}{\pi m} \right)^{1/2} e^{\frac{e\Phi_s}{kT_e}} + \frac{1}{2} \sqrt{\frac{kT_e}{M}} (\varepsilon - \Phi_s) \right] \tag{4}$$

$$P_a = 2T_{\mathrm{eV}} I_a \approx 2T_{\mathrm{eV}} I_d \tag{5}$$

$$P_R = n_o n_e \langle \sigma_* v_e \rangle V_p \tag{6}$$

$$P_i = (I_b + I_{iw}) U^+ = [\eta_b + I_{ew}(1 - \gamma)] I_d U^+ \tag{7}$$

where V_b is the beam voltage, I_b is the beam current, e is the charge of an electron, A_w is the surface area of the inner and outer discharge channel walls in contact with the plasma, k is the Boltzmann constant, m is the mass of an electron, Φ_s is the sheath potential relative to the plasma, M is the mass of a xenon atom, ε is the presheath ion energy, T_{eV} is the electron temperature in electron volts, I_a is the current to the anode, I_d is the discharge current, n_o is the neutral density, $\langle \sigma_* v_e \rangle$ is the excitation reaction rate coefficient including the excitation cross section and the electron velocity, V_p is the volume of the high-temperature plasma region, I_{iw} is the ion current to the walls, U^+ is the ionization potential, η_b is the beam current utilization efficiency, I_{ew} is the electron current to the walls, and γ is the secondary electron yield.

To complete this analysis, several assumptions were made. The anode-region electron temperature was assumed to be 4 eV and the axial depth of the high-density plasma near the exit-region of the thruster was assumed to be 3 mm. The current and voltage efficiencies were assumed to be 70% and 90%, respectively, and the magnetic field strength at the peak field point was conservatively assumed to be 160 G. A discharge current of 1.3 A and a total propellant flow rate of 20 sccm were also assumed. Using these assumptions and the known MaSMi thruster dimensions, the various power loss terms presented in (3)–(7), in addition to the beam power and the electron temperature, were calculated as functions of the discharge voltage.

The beam power, the net power carried by the plasma beam, is approximately 245 W according to the unshielded power model (2)–(7). The power deposited to the channel walls is broken into two terms: the first is the power deposition of electrons that overcome the repelling sheath potential and the second is the power deposition of ions that fall through the presheath and sheath potentials (the cooling effect of emitted

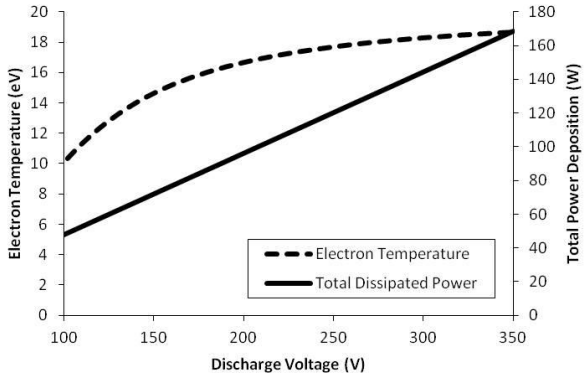

Fig. 4. Electron temperature and total power deposition as a function of discharge voltage calculated for an unshielded 44-mm Hall thruster operating at 1.3 A discharge current.

secondary electrons is neglected). Electron and ion heating of the walls account for approximately 115 and 4 W, respectively, of the total 145 W of power dissipated to the discharge channel walls in an unshielded MaSMi thruster. The remaining 25 W are contributions from xenon ionization, electron power deposition to the anode, and radiation. The xenon ionization power is 12.6 W and is not sensitive to changes in the thruster model's operation conditions. The power deposited to the anode is calculated based on the assumption that the discharge current is effectively equal to the electron current collected at the anode and assumes that the plasma potential is equal or slightly higher than the anode potential. Electrons are assumed to deposit $2T_{\mathrm{eV}}$ of energy from the plasma to the anode, totaling in ∼10.5 W of power loss for the unshielded model. The radiative power loss is the thermal power radiated by the plasma volume (the product of the discharge channel cross-sectional area and the axial thickness of the high-temperature plasma region) based on the excitation of neutrals in the plasma. Radiative power losses for the unshielded thruster total to ∼2.5 W. The power to produce ions is the sum of the power used to generate the beam ions (product of the beam current and the ionization potential) and the power used to create ions that will bombard the discharge channel walls (product of the ion current to the walls and the ionization potential). Alternatively, this power can be calculated based on the beam efficiency and the electron current to the discharge channel walls, accounting for emitted secondary electrons; the sum of these factors is multiplied by the discharge current and ionization potential. Ionization power to the beam and wall ions totals to ∼17 W for the unshielded thruster model. Other terms, including the power electrons may carry into the beam, are generally small and can be neglected [14].

For MaSMi's original expected operating conditions (300 V, 1.3 A), the electron temperature is calculated to be approximately 18.3 eV with a total power deposition of approximately 145 W according to the power model (calculated for conventional unshielded Hall thrusters). Fig. 4 shows the electron temperature and total power deposition to the discharge channel walls and anode for a variety of discharge voltages at the expected operation discharge current of 1.3 A. An additional 35 W of power is expected to be generated by the two magnetic coils during nominal operation based on a temperature-sensitive model relating applied current and resulting magnetic field strength. The 180 W of thermal power predicted by this model represents an important challenge that must be considered carefully for thruster and mission design efforts.

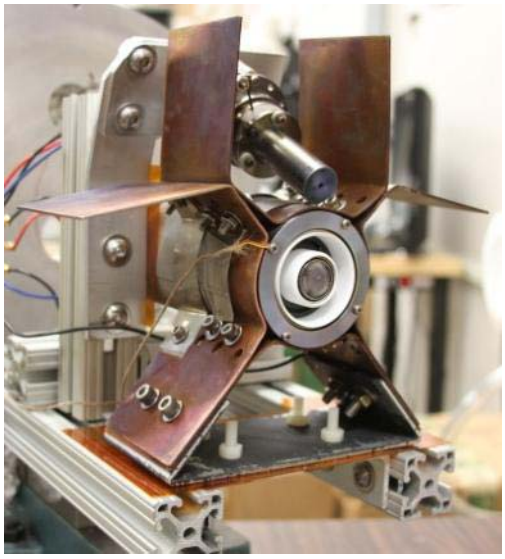

Fig. 5. MaSMi Hall thruster fitted with thermal radiator and cathode.

2) Thermal Model: A thermal balance was performed to determine MaSMi's temperature during operation based on the power deposition model presented above. This balance, only accounting for thermal radiation, is represented by

$$Q_{\mathrm{int}} = \sigma \varepsilon_R A_R F \left(T_M^4 - T_s^4\right) \tag{8}$$

where Q_{int} is the power lost from plasma-heating of the thruster, σ is the Stephan-Boltzmann's constant, ε_R is the surface emissivity, A_R is the radiation surface area, F is the free-space-facing view factor (assumed to be 1 in our case), T_M is MaSMi's mean surface temperature, and T_s is the temperature inside the vacuum chamber (assumed to be room temperature). Assuming no conduction, a total plasma heating power loss of 180 W, an emissivity of 0.3 (bare Hiperco), and a radiation area equal to the surface area of the thruster body, the predicted operation temperature is 450 °C, which exceeds the thermal rating of the insulated magnet wire (∼400 °C). To efficiently dissipate the predicted 180 W, a thermal radiator is fitted over the thruster's outer core. The radiator is constructed from four 1.59-mm thick copper sheets with a quarter-circular bend in the center and bolted together tightly in the shape of an X to ensure thermal contact with the thruster body. The two upper fins are spread apart for greater surface area. The radiator, with a total space-viewing surface area of ∼1000 cm^2, is oxidized (emissivity ∼ 0.75) to yield a predicted thruster operation temperature of ∼195 °C. A photograph of the MaSMi Hall thruster mounted in its thermal radiator is presented in Fig. 5.

3) Separatrix Analysis: Conventional Hall thrusters generally have one of two magnetic coil configurations to achieve the desired field topology. The first configuration uses discrete outer coils located at multiple, equally spaced azimuthal

locations oriented parallel to the thruster's axis. These coils are magnetically coupled to the thruster's magnetic core to complete the thruster's magnetic circuit. The second thruster configuration uses a single outer coil, concentric with the thruster's discharge channel and oriented along the thruster's axis. This single coil is generally sheathed by the thruster's outer core to connect the coil to the thruster's magnetic circuit. In either design, a single inner magnet coil located radially inward from the inner wall of the discharge channel may be implemented.

Thrusters using discrete outer coils generate two species of field lines that extend outside of the thruster body. The first circulates through the magnetic circuit and then travels from the inner pole to the outer pole. The second extends from the front of the outer coils and then reconnects at the back of the coils, traveling around the thruster body (not conducted by the magnetic circuit). Thrusters using a single outer coil generate only one magnetic field line species that extends outside the thruster body. These field lines travel from the thruster's inner pole and reconnect at the outer pole, sides, and rear of the thruster body to be circulated through the thruster's magnetic circuit.

The placement of the thruster's hollow cathode is a critical design feature depending on a thruster's magnetic coil configuration. Work is necessary for electrons born from the cathode to travel to the anode and ion beam, overcoming both strong magnetic fields and insufficient collision frequency, to maintain charge quasi-neutrality. The minimization of this power, which can be considered an energy loss mechanism, results in more effective cathode coupling with the thruster and improved thruster efficiency [31], [32]. In the case of a Hall thruster with discrete outer coils, the magnetic field is divided into two regions of similarly connected flux lines (the two different species of flux lines discussed above); the boundary between these regions is called the separatrix. In a series of cathode coupling investigations using a BPT-2000 Hall thruster (which uses four discrete outer coils), Sommerville and King [31], [32] determined that placing a Hall thruster's hollow cathode orifice within the separatrix (toward the thruster's centerline) yielded significantly better thruster efficiency and improved cathode coupling.

In an effort to examine cathode coupling, MaSMi's far-field magnetic field structure was simulated to determine the location of the separatrix. Consistent with Sommerville's findings, the fields model suggests that that no separatrix exists in MaSMi's external magnetic field structure, as shown in Fig. 6 [32]. Based on this observation, cathode placement should not be a major concern for strong cathode coupling and efficient operation of the MaSMi Hall thruster.

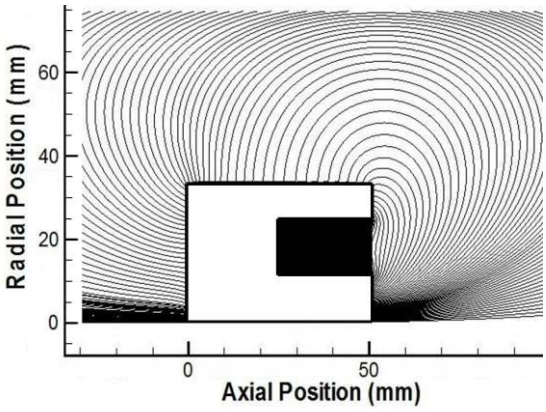

Fig. 6. Simulation of MaSMi's external magnetic field structure confirming that no separatrix is present.

Fig. 7. UCLA electric propulsion test facility.

IV. Experiment Configuration

A. Vacuum Facility and Supporting Equipment

Experiments were carried out in the Electric Propulsion Test Facility in the Plasma and Space Propulsion Laboratory at UCLA. The UCLA Electric Propulsion Test Facility, shown in Fig. 7, uses a custom built cylindrical chamber measuring 2.8-m long with a diameter of 1.8 m. Two CTI CryoTorr-10 cryogenic pumps operate in parallel for a combined xenon pumping speed of ∼1300 l/s. This system is capable of achieving a base pressure of approximately 5×10^{-7} torr, and during nominal operation with an approximate xenon flow of 12 sccm, the chamber pressure remained in the mid 10^{-5} torr range (corrected for xenon).

The five power supplies required for normal operation of the MaSMi Hall thruster and supporting hollow cathode were installed on a power supply rack adjacent to the Electric Propulsion Test Facility vacuum chamber. MaSMi's anode potential was provided by a Sorensen DLM 300-2 power supply while the inner and outer magnet coils were powered by a pair of Sorensen DLM 20-30 power supplies. Sorensen DLM 40-15 and DLM 150-4 power supplies were used for the hollow cathode's heater and keeper, respectively. Research grade xenon was supplied to the thruster by an Apex AX-DM 50 sccm mass flow controller and to the cathode by an Apex AX-DM 5 sccm mass flow controller.

MaSMi was coupled to a BaO-W cathode based on the ISS plasma contactor cathode and the NSTAR ion thruster cathode. The cathode has a 0.75 mm diameter cathode orifice and a tantalum keeper with a 3-mm diameter orifice. All other dimensions are similar to the NSTAR hollow cathode. During initial testing, the cathode was mounted parallel to the thruster axis with the cathode orifice ∼6.6 cm (1.5 channel outer diameters) above the thruster centerline. Although cathode coupling in this configuration was sufficient to operate the thruster, the thruster and cathode did not demonstrate consistent discharge stability, which was contrary to earlier coupling predictions based on the above separatrix arguments. In an effort to enhance cathode coupling, MaSMi's cathode was later mounted at a 22.5° angle relative to the thruster's centerline axis with the Orifice ∼10 mm above the thruster body in the plane of the thruster face and directed toward the beam. This second configuration yielded superior stability during thruster operation and was maintained throughout all ensuing performance characterization testing.

A high energy beam dump, consisting of a 1.25 m × 1.25 m square of 1.59-mm carbon felt mounted to a grounded aluminum frame, was mounted 80 cm downstream of the MaSMi Hall thruster. The close proximity of the beam dump to the thruster was selected to provide a short path for energetic carbon atoms ejected from the felt to easily backsputter onto the thruster discharge channel, enabling a visual verification of a successfully shielded thruster.

B. Diagnostics

In its current configuration, the UCLA Electric Propulsion Test Facility employs two thruster plume characterization diagnostics: a retarding potential analyzer (RPA) and a scanning planar probe. Further diagnostics necessary to fully measure MaSMi's performance (i.e., $\mathbf{E} \times \mathbf{B}$ analyzer, emissive probe, Faraday probe, etc.) are under construction. It should be noted that due to the small dimensions of the discharge channel and in an effort to leave the discharge plasma undisturbed during testing, invasive probe diagnostics were not used. Instead, a future computational investigation using Hall2De, with complementary experiments, will be conducted to examine the plasma behavior inside MaSMi's discharge channel [11], [18], [19].

1) Scanning Planar Probe: A scanning planar probe, comprised of a flat, circular, single-sided electrode with a negative voltage bias, is used to determine the ion current density and integrated beam current. The current density (J_i) is calculated as $J_i = I_p/A_p$ where I_p is the ion current collected by the probe and A_p is the probe area. The total beam (ion) current is determined by integrating the current density azimuthally around the beam profile. Because a single probe scan measured the ion current from each side of the thruster, the ion current at each location is integrated around half of the azimuthal distance of the beam and then summed to account for any slight asymmetries in the beam profile. This simplifies to

$$I_b = \pi w \sum J_{i,n} R_n \tag{9}$$

where w is the width of the beam sampled by the probe (equal to the resolution of the scan) and R_n is the nth lateral distance of the probe from the thruster's centerline (in the plane of the probe trace).

The planar probe used was an alumina-insulated 1.27-mm diameter tantalum wire with a 3.97-mm diameter, 0.13-mm thick molybdenum disk. The planar probe was scanned laterally ±12 cm from the thruster's centerline and mounted 4.4 and 10.8-cm downstream of the thruster face (see Fig. 8). The 4.4-cm probe scan was used for ion current density measurements because charge exchange effects are minimized near the thruster while the 10.8-cm scan offered insight into the evolution of the plume's properties downstream of the thruster. The probe's electron-repelling bias was measured as −28 V relative to the chamber potential. A Velmex single-axis mechanical translation stage with supporting stepping motor controller provided horizontal motion across the thruster face at the set axial distance.

2) Retarding Potential Analyzer: ARPA uses a series of biased grids to measure ion energy. The first grid is in contact with the plasma and floats relative to the plasma potential. The second grid is negatively biased to repel electrons, preventing them from entering the RPA and being collected by the ion collector electrode. The third (and sometimes fourth) grid is used as a positively biased ion discriminator, allowing only ions with energies greater than the applied voltage to reach the collector. The ion energy distribution is obtained by taking the first derivative of the current collected by the collector plate with respect to voltage [33].

The RPA built for this facility has a 9.53-mm diameter entrance orifice to the grid assembly. It uses stainless steel grids, each mounted to a 0.51 mm stainless steel ring; the individual plasma, electron repeller, and ion discriminator grid transparencies are 36%, 44%, and 40%, respectively. The RPA employs a four-grid design where the third and fourth grids, making up the ion discriminator, act as a double-discriminator (therefore, the effective grid transparency of the ion discriminator is 0.16). A four-grid design improves the energy resolution of the probe while preventing reductions in the discriminator potential at the centers of the ion grid orifices, which may permit lower energy ions through the grid and lead to an overestimated ion current for a given discriminator potential [34]. At the end of the assembly is a 0.77-mm thick, stainless steel disk as a simple collector plate. Each grid is separated by a 0.38-mm insulator ring, and the entire assembly is insulated from the aluminum RPA body by a cylindrical insulator. The RPAs electron repelling grid was biased to −28 V relative to ground while the ion discriminator grid's swept potential was provided by an Acopain P10HP60 high voltage power supply. The RPA was mounted on (and grounded to) the frame of the high-energy beam dump, fixed 80 cm axially downstream of MaSMi's centerline, as shown in Fig. 8.

3) Thermocouples: Four omega K-type thermocouples were mounted on MaSMi to monitor operational temperatures. Three thermocouples were held at the base of the discharge channel and approximately equally spaced in the azimuthal

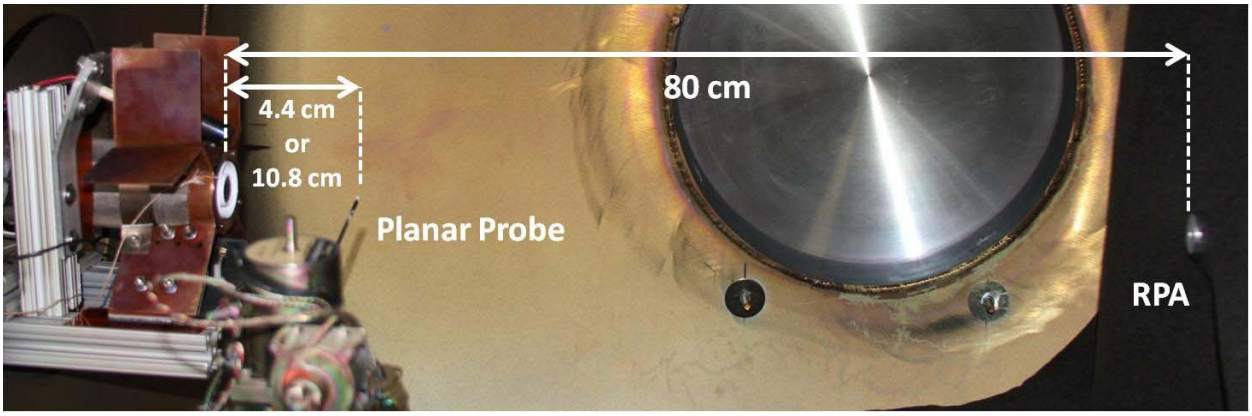

Fig. 8. Planar probe and RPA locations downstream of the MaSMi Hall thruster.

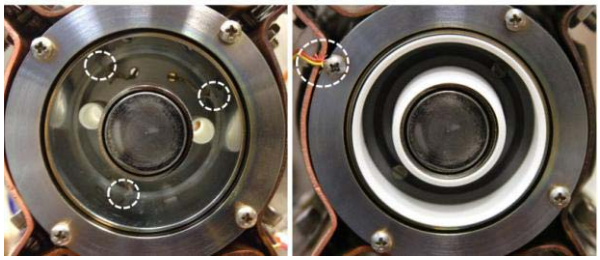

Fig. 9. MaSMi thermocouple placement behind the discharge channel (left) and on the outer pole piece (right).

direction (Fig. 9, left); the fourth was mounted on the outer pole piece, below and to the left of the cathode (Fig. 9, right). Temperatures were measured with Fluke digital multimeters.

V. Results and Discussion

The initial performance characterization experiments for the MaSMi Hall thruster were conducted at a discharge voltage of 275 V and a discharge power of 325 W. Early operation point optimization began at 300 V and 1.3 A in an effort to achieve the original design point of 390 W; however, testing revealed that the final operation conditions (275 V and 325 W) yielded a more stable discharge and constant temperatures throughout the duration of a given test. It should be noted that the nominal operation point is nearly identical to the predicted discharge power suggested by scaling laws used prior to thruster fabrication (Section III-A).

The anode propellant flow rate was set to 10.75 sccm of xenon while the cathode propellant flow rate was set to 1.1 sccm (10% of the anode flow rate). The inner and outer magnet coils were operated at 5.2 and 1.5 A, respectively. Average operational temperatures of approximately 450 °C and 475 °C were measured at the base of the discharge channel and at the front pole piece, respectively. The thruster performance was measured during eight experimental trials with a total run-time of approximately 4 h during this initial testing period.

Two minor cracks in the thruster parts occurred during the final stages of testing (after the operation point was optimized to 325 W). The first was an axial crack along the outer wall of the discharge channel and the second was a radial crack on the inner graphite ring of the anode (Fig. 11). Although their cause is under investigation, it is likely due to anode thermal expansion that will be corrected during the next phase of performance testing. The operation of the MaSMi thruster at the nominal operation point was unaffected by these cracks and testing was concluded before the parts were replaced.

A. Magnetic Shielding

A photograph of the MaSMi Hall thruster during operation, with a magnified view of the upper discharge channel is presented in Fig. 10. To the naked eye, the plasma discharge appears to be slightly offset from the outer channel wall and more concentrated toward the center of the discharge channel. The offset indicates a significantly lower neutral excitation rate near the channel surfaces, suggesting that only low temperature plasma is interacting with the walls. Similar to the visual observations with the H6MS, this was the first evidence suggesting that MaSMi achieved a magnetically shielded field topology [10]. The brightness of the discharge and the small scale of the thruster make it difficult to visually determine if the discharge was similarly offset from the inner wall.

A visual inspection of MaSMi's inner and outer discharge channel walls was conducted after each performance test. Fig. 11 shows a comparison of MaSMi's discharge channel before and after testing. An even coating of carbon had been deposited on the outer wall of the discharge channel along its full axial length and covering the chamfered exit region; no exposed BN was visible anywhere on the outer channel wall. The inner wall of the discharge channel was found to be noticeably darker (more gray) in color than it was before testing, suggesting some carbon deposition in this region. Thin exposed rings of clean BN were found along the edges of the chamfers on the inner wall near the downstream edge; however, the remaining surface area near the thruster exit had an obvious dusting of carbon, suggesting that weaker magnetic shielding was present.

The thick carbon coating of the outer wall suggests that the backsputter rate of carbon from the high-energy beam dump exceeded the ion sputter rate of the outer wall material. The inner wall also showed evidence that

Fig. 10. Operation of MaSMi at 275 V and 325 W with a magnified view of the upper region of the discharge channel showing a slight offset of the plasma from the wall typical of magnetic shielding.

Fig. 11. Comparison of MaSMi's discharge channel before (left) and after (right) testing. The layer of carbon back-sputter suggests the presence of magnetic shielding.

plasma–wall interactions had been reduced; however, localized magnetic circuit saturation was likely the cause of the weaker shielding of the inner wall. In an effort to bound the erosion rate of the thruster's discharge channel, a back-sputter calculation was performed to determine the rate of carbon redeposition on the discharge channel downstream-facing edges (the area of the most concentrated ion bombardment erosion).

According to the literature, the erosion rate of the BN discharge channel under xenon-ion bombardment ($\varepsilon_{\mathrm{Xe-BN}}$) is bounded by

$$\begin{aligned}\varepsilon_{\mathrm{Xe-BN}} &\leq \alpha R_C \left(\frac{\rho_C m_{\mathrm{BN}}}{\rho_{\mathrm{BN}} m_C}\right)\left(\frac{Y_{\mathrm{Xe-BN}}}{Y_{\mathrm{Xe-}C/\mathrm{BN}}}\right) \\ &\approx 2R_C\left(\frac{Y_{\mathrm{Xe-BN}}}{Y_{\mathrm{Xe-}C/\mathrm{BN}}}\right) \end{aligned} \tag{10}$$

where α is the sticking coefficient (assumed to be unity), R_C is the carbon backsputter rate, ρ_C is the mass density of carbon, m_{BN} is the particle mass of BN, ρ_{BN} is the mass density of BN, m_C is the particle mass of carbon, $Y_{\mathrm{Xe-BN}}$ is the sputter yield of BN under xenon ion incidence, and $Y_{\mathrm{Xe-}C/\mathrm{BN}}$ is the sputter yield of carbon-coated BN under xenon ion incidence [10]. The sputter yield of carbon from the high energy beam dump was 7.2×10^{-2} atoms/ion, calculated using the methods for carbon material sputtering presented by Tartz and assuming perpendicular ion incidence to the beam dump [35]. The ion beam was assumed to strike the beam dump in a circular profile of radius 50 cm, calculated based on the beam divergence half-angle of 30° originating from the thruster channel's outer wall (the divergence half-angle calculation is shown in Section V-B2 below). Approximated 4.7×10^{17} carbon atoms/s were ejected from the beam dump, calculated by converting the measured ion current into number of ions incident on the dump per second and then multiplying by the sputter yield. A view factor was calculated from each of the discharge channel downstream edges' projected areas (two concentric annuli with thicknesses equal to that of the discharge channel walls) to the projected beam area, resulting in a view factor of 5.5×10^{-5} and 9.7×10^{-5} for the inner and outer edges, respectively. Multiplying these view factors by the number of carbon atoms ejected from the beam dump gives the total number of carbon atoms expected to be deposited on the channel's downstream edges, yielding 2.6×10^{13} and 4.6×10^{14} atoms/s for the inner and outer edges, respectively. Assuming an average distance between the sputter-deposited

carbon atoms' nuclei of 140 pm, the number of atoms required to yield a 1-μm thick layer on the inner and outer edges' projected areas are 5.6×10^{19} and 9.7×10^{19} atoms/μm, respectively. The product of the inverse of these values and the number of carbon atoms deposited on the channel edges per second gives a total carbon deposition rate of approximately 1.7×10^{-3} μm/h for both the inner and outer discharge channel edges.

Applying this result to (10) gives a maximum channel erosion rate is approximately 3×10^{-2} μm/h where the sputter yield ratio is conservatively assumed to be 10, as discussed in [10]. Although the simplifying assumptions for these erosion rates yield a very large uncertainty, the reported values are approximately three orders of magnitude below common erosion rates of unshielded Hall thrusters [10], [12], [16]. Therefore, an error of several orders of magnitude in the calculated erosion rate (which is possible, however, unlikely, due to the applied calculation method) still demonstrates a significant improvement over unshielded Hall thrusters.

B. Performance

1) Theory: In addition to the useful life of the device (discussed above), the key figures of merit for the MaSMi Hall thruster are thrust, specific impulse, and efficiency. The thrust (T) is given by

$$T = \sum_i \dot{m}_i \langle v_i \rangle = \eta_b I_d \sqrt{\frac{2MV_d\eta_v\eta_d}{e}} \sum_i \frac{f_i}{Z_i} \tag{11}$$

where $\dot{m}_i$ is the ion mass flow rate, $\langle v_i \rangle$ is the average ion velocity, V_d is the discharge voltage, η_v is the beam voltage utilization efficiency, η_d is the plume divergence efficiency, Z_i is the charge state of the ith ion species, and f_i is the current fraction of the ith species given by

$$f_i = \frac{I_i}{I_b} \tag{12}$$

where I_i is the current of the ith ion species the efficiencies in (11) are defined below. The correction term in (11), which accounts for the presence of multiply charged species in the ion beam, can be calculated for any number of ion charge states as

$$\sum_i \frac{f_i}{Z_i} = \frac{I^+ + \frac{1}{2}I^{++} + \frac{1}{3}I^{+++} + \cdots}{I_b} \tag{13}$$

where I^+, I^{++}, and I^{+++} are the currents of singly, doubly, and triply ionized particles in the plasma beam.

The specific impulse (I_{sp}) is given by

$$I_{\text{sp}} = \frac{T}{\dot{m}_a g} = \frac{\eta_m}{g}\sqrt{\frac{2eV_d\eta_v\eta_d}{M}} \left(\frac{\sum_i \frac{f_i}{\sqrt{Z_i}}}{\sum_i \frac{f_i}{Z_i}} \right) \tag{14}$$

where $\dot{m}_a$ is the thruster anode mass flow rate, g is the acceleration of gravity at the Earth's surface, η_m is the mass utilization efficiency (defined below), and

$$\sum_i \frac{f_i}{\sqrt{Z_i}} = \frac{I^+ + \sqrt{\frac{1}{2}}I^{++} + \sqrt{\frac{1}{3}}I^{+++} + \cdots}{I_b}. \tag{15}$$

The total efficiency (η_T) is the ratio of the jet power (P_{jet}) in the thruster exhaust to the total thruster input power:

$$\begin{aligned} \eta_T &= \frac{P_{\text{jet}}}{P_T} = \left(\frac{T^2}{2\dot{m}_a P_d}\right)\left(\frac{\dot{m}_a}{\dot{m}_T}\right)\left(\frac{P_d}{P_T}\right) \\ &= \eta_a\eta_c\eta_o = \eta_{\text{tc}}\eta_o \end{aligned} \tag{16}$$

where P_T is the total thruster input power (sum of the discharge, magnet, and keeper powers), $\dot{m}_T$ is the total propellant flow rate (sum of the anode and cathode flow rates), η_a is the anode efficiency, η_c is the cathode efficiency, η_o is the electrical utilization efficiency, and η_{tc} is an effective thruster efficiency consisting of the efficiency contributions of the thruster and cathode only.

The anode efficiency can be broken into the product of five utilization efficiencies given by

$$\eta_a = \frac{T^2}{2\dot{m}_a P_d} = \eta_v\eta_b\eta_m\eta_d\eta_q \tag{17}$$

where the utilization efficiencies for the beam voltage, beam current, mass, plume divergence, and charge (η_q) are

$$\begin{aligned} \eta_v &= \frac{V_b}{V_d}, \quad \eta_b = \frac{I_b}{I_d} \\ \eta_m &= \frac{\dot{m}_b}{\dot{m}_a} = \frac{MI_d}{\dot{m}_a e}\eta_b \sum_i \frac{f_i}{Z_i} \\ \eta_d &= (\cos\theta)^2, \quad \eta_q = \frac{\left(\sum_i \frac{f_i}{\sqrt{Z_i}}\right)^2}{\sum_i \frac{f_i}{Z_i}}. \end{aligned} \tag{18}$$

In (18), $\dot{m}_b$ is the beam propellant flow rate and θ is the plume divergence half-angle. The cathode, electrical utilization, and effective thruster efficiencies are given as

$$\begin{aligned} \eta_c &= \frac{\dot{m}_a}{\dot{m}_a + \dot{m}_c} = \frac{\dot{m}_a}{\dot{m}_T} \\ \eta_o &= \frac{P_d}{P_T} = \frac{V_d I_d}{V_d I_d + P_{mag} + P_k} \\ \eta_{\text{tc}} &= \eta_a\eta_c \end{aligned} \tag{19}$$

where $\dot{m}_c$ is the cathode mass flow rate, P_{mag} is the magnet power, and P_k is the keeper power.

Due to the relatively high background pressures observed during thruster operation, a method for compensating for neutral gas entrained into the thruster channel was implemented [36]. The entrained mass flow ($\dot{m}_{en}$) is given by

$$\dot{m}_{en} = A_{en}\frac{n_n M}{4}\left(\frac{8kT_n}{\pi M}\right)^{1/2} = A_{en}P\left(\frac{M}{2\pi kT_n}\right)^{1/2} \tag{20}$$

where A_{en} is the entrainment area approximated as a hemisphere with a radius equal to the discharge channel outer diameter, T_n is the temperature of the background neutral particles, and P is the facility pressure. This entrained mass flow can then be converted to account for entrained discharge current (I_{en}) given by

$$I_{en} = \dot{m}_{en}\frac{e}{M} \tag{21}$$

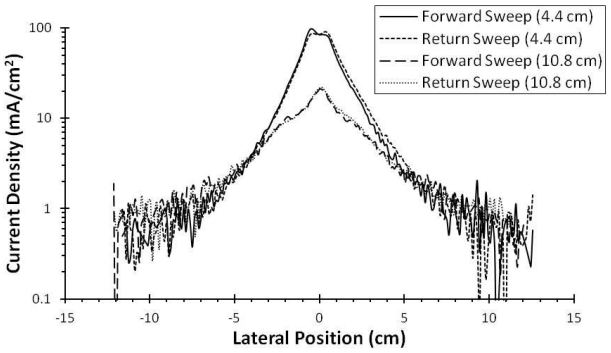

Fig. 12. Current density as a function of the planar probe's lateral position from the thruster centerline, uncorrected for background charge exchange ion effects and measured for nominal MaSMi operating conditions at 4.4 and 10.8-cm downstream of the thruster face.

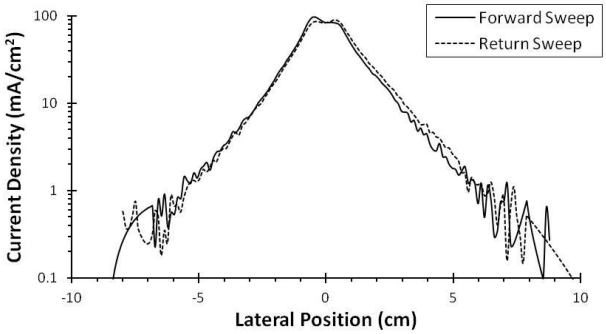

Fig. 13. Current density as a function of the planar probe's lateral position from the thruster centerline, corrected for background charge exchange ion effects and measured for nominal MaSMi operating conditions at 4.4-cm downstream of the thruster face.

where it is assumed that the neutral particles are singly ionized. These corrections can be applied to the measured discharge current and anode flow rate as

$$I_{d,true} = I_d - I_{en}, \quad \dot{m}_{a,true} = \dot{m}_a + \dot{m}_{en} \tag{22}$$

where the subscript true represents the corrected value. The entrained mass correction for thrust (T_{true}) is given by

$$T_{true} = T\left(1 - \zeta_{en}\frac{\dot{m}_{en}}{\dot{m}_{a,true}}\right) \tag{23}$$

where ζ_{en} is the entrained mass utilization factor used to account for ingested neutrals that were ionized but that did not contribute to useful thrust. The value of the entrained mass utilization factor is 0.5 according to [36]. The corrected specific impulse ($I_{sp,true}$) can then be calculated from (14) using the corrected thrust (23) and the measured anode propellant flow rate because only the thrust term is dependent on the facility pressure. Using the corrected thrust and specific impulse, a corrected total efficiency ($\eta_{T,true}$) can be calculated using a modified form of (16) given as

$$\eta_{T,true} = \left[\frac{g}{2}\left(\frac{I_{\text{sp},true}T_{true}}{P_{T,true}}\right)\right]\eta_{o,\text{true}}\eta_{c,true} \tag{24}$$

where $P_{T,true}$, $\eta_{c,true}$, and $\eta_{o,true}$ are given by

$$\begin{aligned} P_{T,true} &= V_d I_{d,true} + P_{mag} + P_k \\ \eta_{c,true} &= \frac{\dot{m}_{a,true}}{\dot{m}_{a,true} + \dot{m}_c} \\ \eta_{o,true} &= \frac{V_d I_{d,true}}{P_{T,true}}. \end{aligned} \tag{25}$$

2) Planar Probe Results: The current density measured by the planar probe at both the 4.4 and 10.8-cm downstream locations as a function of the probe's lateral position from the thruster centerline is presented in Fig. 12. Both the forward and return sweeps are shown for each axial distance to demonstrate repeatability of the measurement.

The ion current was determined from the 4.4-cm downstream planar probe trace because charge exchange effects are reduced, but not eliminated, near the thruster face (in this case, one discharge channel diameter downstream). A correction is therefore necessary to account for facility background charge exchange ion effects, which exist both in the wings of the probe trace as well as near the thruster centerline [10]. This was accomplished by first determining the average value of the ion current density from ± 7 to ± 12 cm laterally away from the thruster centerline (encompassing the wings of the trace), which was $\sim$0.68 mA/cm^2. This value was then subtracted from each ion current density measurement to account for effects of background charge exchange ions across the entire probe trace. The calculated ion current using this charge exchange correction was slightly more conservative than using an exponential curve generated for the data collected near the thruster axis and extended to the limits of the data collection range, which is an alternative method suggested in [37]. The corrected ion current density as a function of the probe's lateral position for the thruster centerline is shown in Fig. 13. Again, both the forward and return sweeps are presented to show measurement repeatability.

The ion current, calculated from (9) and based on the current density measurement corrected for background charge exchange ion effects, was 1.04 A. Several methods were employed to determine the approximate uncertainty of this measurement. Sheath expansion effects were considered based on the studies of probe–plasma interactions by Sheridan; however, the results presented are applicable to a double-sided flat probe in a stationary plasma [38]. Because the ions in a Hall thruster discharge comprise a flowing plasma (in the order of 10 s of km/s) and the planar probe utilized was single sided, it was assumed that sheath expansion effects were negligible. Additionally, the probe was observed to be cooler than the temperature required for significant electron current emission. The beam current utilization efficiency, calculated using (18), was therefore found to be 88% with an uncertainty of approximately $+2\%/-8\%$ related to the planar probe measurement.

The plume divergence angle was approximated by determining the portion of the beam that contained 95% of the total current (corrected for charge exchange). A beam divergence half-angle of approximately 30° was observed, yielding a plume divergence efficiency of 75% (18) with an uncertainty of approximately $+2\%/-8\%$ based on the planar probe measurement.

3) RPA Results: The ion current collected from the RPA traces is presented in Fig. 14; both the normalized ion current and its normalized derivative with respect to voltage is

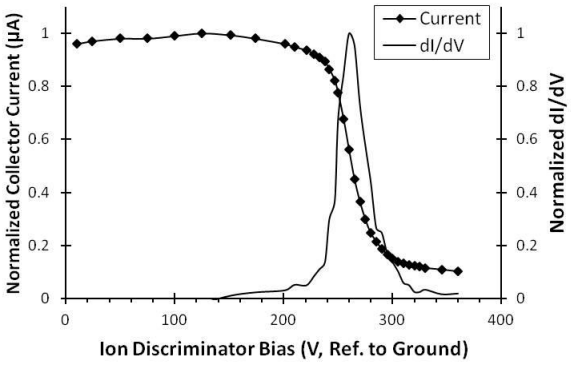

Fig. 14. RPA scans of normalized ion current and its normalized derivative as functions of the ion discriminator grid potential for MaSMi's nominal operating condition.

presented as functions of the ion discriminator grid bias for the nominal operation point of the MaSMi Hall thruster.

The most probable ion potential measured directly from the RPA was approximately 261 V; however, this value must be corrected to account for the plasma potential at the RPA location (the RPA body was grounded during this test). The floating potential was measured from the RPAs plasma grid during each thruster test and values were approximately 1 V. Because an emissive probe was unavailable to directly measure the plasma potential at the RPA location, a series of assumptions were made to determine this value. First, a local electron temperature of 3 eV was assumed at the RPA location; this relatively high value was selected to maintain a conservative estimate of the plasma potential. Second, the plasma potential was approximated by equating the electron current with the fast (beam) and slow (charge exchange) ion currents local to the RPA, taking the form of

$$\frac{1}{4}n_e e A_{RPA}\sqrt{\frac{8kT_e}{\pi m}}e^{-\frac{e\Phi}{kT_e}} = eA_{RPA}\left(\frac{1}{2}n_{i,slow}\sqrt{\frac{kT_e}{M}}+n_{i,fast}\sqrt{\frac{2e\eta_v V_d}{M}}\right) \quad (26)$$

where A_{RPA} is the area of the RPA orifice, $n_{i,slow}$ is the slow ion density, and $n_{i,fast}$ is the fast ion density. The fast ion density near the RPA was approximated based on the plasma density calculated from the planar probe measurements taken at 4.4 and 10.8-cm downstream of the thruster and then extrapolated for a 30° plume expansion based on the ratio of the beam area at the two downstream locations. The centerline values of the plasma density were used for this calculation as the RPA was located axially downstream of the thruster. This resulted in a plasma density reduction factor of approximately 1.6×10^{15} m^{-1} divided by the beam area at a given downstream location, yielding a fast ion density of 2.4×10^{15} m^{-3} near the RPA. The slow ion density was calculated based on equating the rate of charge exchange ion production in the beam and the rate of ions lost from the beam traveling at the Bohm velocity. The resulting slow ion density was several orders of magnitude smaller than the fast ion density and was neglected, which allowed for the assumption of quasi-neutrality ($n_e \approx n_{i,\text{fast}}$). The voltage utilization efficiency was initially guessed and then iterated on simultaneously with the plasma potential, Φ (note that (26) is a function of both the plasma potential and the voltage utilization efficiency). The result was a calculated plasma potential of 8 V, or roughly $3T_e$, above the local floating potential. Subtracting the calculated plasma potential and 1 V floating potential from the RPA-measured ion energy results in a most probable ion potential of 252 V; an approximate uncertainly of the plasma potential of $2T_e$ (6 V) was assumed. Applying these values to (18), a voltage utilization efficiency of 92% is achieved with an uncertainty of approximately ±3%.

4) Efficiency, Thrust, and Specific Impulse: To calculate MaSMi's total efficiency, the ion beam composition must be assumed (recall that $\mathbf{E} \times \mathbf{B}$ probe measurements were unavailable at the time of testing). Conventionally, unshielded miniature Hall thrusters of the same scale as MaSMi generate favorable ion species mixes. The BHT-200-X3, for example, produces approximately 95.5% singly charged, 3.7% doubly charged, and 0.8% triply charged ions [39]. By contrast, the H6MS Hall thruster generates a species mix of 57.5% singly, 25.9% doubly, and 16.6% triply and quadruply charged ions [10]. In an effort to maintain conservative results, MaSMi's beam was assumed to be composed of three ion charge states and that the species mix was equal to that produced by the H6MS.

Using the H6MS species mix, the mass utilization efficiency was calculated using (18). This resulted in a mass utilization efficiency of 102% with an assumed uncertainty of +0%/−10%. The mass utilization efficiency was calculated to be greater than 100% due to uncertainty in the ion current probe measurement and the ion species fractions. The cathode efficiency, calculated as a ratio of the corrected anode flow rate and total propellant flow rate, was approximately 91% with an uncertainty of less than ±1% as reported by the flow controller manufacturer.

MaSMi's electrical utilization efficiency was calculated based on the power supply readings during stable operation. Nominal operation of the thruster occurred at 275 V with a discharge power of 325 W. The hollow cathode keeper, which was left on during all testing to avoid having to restart the cathode heater if the anode discharge went out, was current controlled at 2 A with a power of 40 W. The inner and outer magnet coils operated at 5.2 and 1.5 A, respectively, for a combined power of 29 W. Summing these values, MaSMi's total power was 394 W with an electrical efficiency of 83%. This value has an uncertainty of less than ±1% as reported by the power supply manufacturers.

A summary of MaSMi's total efficiency, including each contributing term from (17), is presented in Table I. The MaSMi Hall thruster demonstrated a calculated total efficiency of approximately 44% with an uncertainty of +5%/−15% (uncorrected for the effects of background neutrals). This corresponds to a thrust of approximately 20 mN at a specific impulse of approximately 1940 s. MaSMi's anode efficiency was approximately 59% with an uncertainty of +6%/−19% while the thruster efficiency (thruster and cathode contributions) was approximately 54% with an uncertainly of +6%/−18%. A summary of the three measures of MaSMi's

TABLE I
SUMMARY OF THE MaSMi HALL THRUSTER'S EFFICIENCY AND ASSOCIATED UNCERTAINTY. TOTAL EFFICIENCY HAS BEEN CORRECTED FOR ENTRAINED BACKGROUND NEUTRALS

	Efficiency	**Uncertainty**
η_b	88%	+2% / -8%
η_v	92%	+/- 3%
η_m	102%	+0% / -10%
η_d	75%	+2% / -8%
η_q	96%	+2% / -8%
η_c	91%	+/- 1%
η_o	83%	+/- 1%
$\boldsymbol{\eta_T}$	**43%**	**+5% / -15%**

TABLE II
SUMMARY OF THE MaSMi HALL THRUSTER'S ANODE, THRUSTER (THRUSTER AND CATHODE CONTRIBUTIONS), AND TOTAL EFFICIENCY WITH ASSOCIATED UNCERTAINTY. TOTAL EFFICIENCY HAS BEEN CORRECTED FOR ENTRAINED BACKGROUND NEUTRALS

	Efficiency	**Uncertainty**
η_a	59%	+6% / -19%
η_{tc}	54%	+6% / -18%
η_T	43%	+5% / -15%

calculated efficiency is presented in Table II. It should be noted that while the calculated thrust matches very well with the prefabrication scaling model's prediction (Section III-A), a significant difference was observed in the predicted and measured specific impulse likely due to multiply charged ion content of the beam not considered in the scaling model.

The values discussed above represent the performance of the thruster without considering the presence of entrained background neutrals and must therefore be corrected. An entrained mass flow of approximately 8.2×10^{-8} kg/s was calculated using (20), yielding an entrained current of approximately 60 mA (21), or 5% of the discharge current. The thrust correction (23) applied to the calculated thrust yields a true thrust of approximately 19 mN, corresponding to a specific impulse of approximately 1870 s. Applying these values to (24) gives a true (or vacuum) total efficiency of 43%. If the total efficiency is calculated using a common beam composition for miniature Hall thrusters (the BHT-200, for example) instead of the more conservative H6MS species mix, the true total efficiency increases significantly.

The total efficiency changed by approximately 1% with the application of the background neutral correction due to the calculated entrained mass flow, which is two orders of magnitude smaller than the measured anode mass flow. Additionally, assuming a $\pm 20\%$ uncertainty in the facility pressure (used to calculate the entrained mass flow) resulted in a change of significantly less than $\pm 1\%$ uncertainty in the thruster's true total efficiency.

VI. CONCLUSION

A 4-cm Hall thruster was developed and tested to demonstrate the application and benefits of magnetic shielding on a miniature scale. The results showed that the MaSMi Hall thruster achieved improved performance values and efficiencies compared with a conventionally unshielded Hall thruster of the same scale while also dramatically improving the projected operational lifetime. For these initial tests, MaSMi exhibited strong shielding of the outer discharge channel wall while the inner channel wall appeared to be weakly shielded. The erosion rate of the shielded discharge channel walls based on carbon redeposition calculations was estimated to be three orders of magnitude less than the measured erosion rates of unshielded Hall thrusters, suggesting a dramatic reduction in ion bombardment erosion and a significant increase in operational lifetime. The total efficiency of the device, accounting for the presence of background neutrals and charge exchange ions, was 43%, corresponding to a thrust of 19 mN and a specific impulse of 1870 s. While testing on a thrust stand is necessary to validate these performance figures, the application and benefits of magnetic shielding was successfully demonstrated on a miniature scale.

REFERENCES

[1] V. Hruby, J. Monheiser, B. Pote, P. Rostler, J. Kolencik, and C. Freeman, "Development of low power Hall thrusters," in *Proc. 30th Plasmadynamics and Lasers Conf.*, Norfolk, VA, USA, Jun. 1999.

[2] A. Smirnov, Y. Raitses, and J. Fisch, "Parametric investigation of miniaturized cylindrical and annular Hall thrusters," *J. Appl. Phys.*, vol. 92, no. 10, pp. 5673–5679, 2002.

[3] W. A. Hargus and C. S. Charles, "Near exit plane velocity field of a 200 W Hall thruster," in *Proc. 39th AIAA/ASME/SAE/ASEE Joint Propuls. Conf.*, Huntsville, AL, USA, Jul. 2003.

[4] B. Beal, A. Gallimore, and W. Hargus, "Preliminary plume characterization of a low-power Hall thruster cluster," in *Proc. 38th AIAA/ASME/SAE/ASEE Joint Propuls. Conf.*, Indianapolis, ID, USA, Jul. 2002.

[5] S. Y. Cheng and M. Martinez-Sanchez, "Hybrid particle-in-cell erosion modeling of two Hall thrusters," *J. Propuls. Power*, vol. 24, no. 5, pp. 987–998, 2008.

[6] D. Jacobson and R. Jankovsky, "Test results of a 200W class Hall thruster," in *Proc. 34th AIAA/ASME/SAE/ASEE Joint Propuls. Conf.*, Cleveland, OH, Jul. 1998.

[7] T. Misuri, F. Battista, and M. Andrenucci, "HET scaling methodology: Improvement and assessment," in *Proc. 44th AIAA/ASME/SAE/ASEE Joint Propuls. Conf.*, Hartford, CT, USA, Jul. 2008.

[8] F. Battista, E. Marco, T. Misuri, and M. Andrenucci, "A review of the Hall thruster scaling methodology," in *Proc. 30th Int. Electr. Propuls. Conf.*, Firenze, Italy, Sep. 2007.

[9] G. Guerrini, C. Michaut, and M. Bacal, "Parameter analysis of three small ion thrusters (SPT-20, SPT-50, A-3)," in *Proc. 2nd Eur. Space Propuls. Conf.*, 1997.

[10] R. Hofer, D. Goebel, I. Mikellides, and I. Katz, "Design of a laboratory Hall thruster with magnetically shielded channel walls, phase II: Experiments," in *Proc. 48th AIAA/ASME/SAE/ASEE Joint Propuls. Conf.*, Atlanta, GA, USA, Aug. 2012.

[11] I. Mikellides, I. Katz, R. Hofer, and D. Goebel, "Design of a laboratory Hall thruster with magnetically shielded channel walls, phase III: Comparison of theory with experiment," in *Proc. 48th AIAA/ASME/SAE/ASEE Joint Propuls. Conf.*, Atlanta, GA, USA, Aug. 2012.

[12] N. Warner, "Theoretical and experimental investigation of Hall thruster miniaturization," M.S. thesis, Dept. Aeronautics Astronautics, Massachusetts Inst. Technol., Cambridge, MA, USA, 2007.
[13] E. Ahedo and J. M. Gallardo, "Scaling down Hall thrusters," in *Proc. 28th Int. Electr. Propuls. Conf.*, Toulouse, France, Mar. 2003.
[14] D. Goebel and I. Katz, *Fundamentals of Electric Propulsion: Ion and Hall Thrusters*. Pasadena, CA, USA: Jet Propulsion Lab., 2008.
[15] T. Ito, N. Gascon, W. Crawford, and M. Cappelli, "Experimental characterization of a micro-Hall thruster," *J. Propuls. Power*, vol. 23, no. 5, pp. 1068–1074, 2007.
[16] K. de Grys, A. Mathers, and B. Welander, "Demonstration of 10,400 hours of operation on a 4.5 kW qualification model Hall thruster," in *Proc. 46th AIAA/ASME/SAE/ASEE Joint Propuls. Conf.*, Nashville, TN, USA, Jul. 2010.
[17] I. G. Mikellides, I. Katz, R. R. Hofer, D. M. Goebel, K. H. De Grys, and A. Mathers, "Magnetic shielding of the acceleration channel in a long-life Hall thruster," *Phys. Plasmas*, vol. 18, no. 1, p. 033501, 2011.
[18] I. G. Mikellides, I. Katz, R. Hofer, and D. Goebel, "Magnetic shielding of walls from the unmagnetized ion beam in a Hall thruster," *Appl. Phys. Lett.*, vol. 102, no. 2, p. 023509, 2013.
[19] I. Mikellides, I. Katz, R. Hofer, D. Goebel, K. de Grys, and A. Mathers, "Magnetic shielding of the channel walls in a Hall plasma accelerator," *Phys. Plasmas*, vol. 18, no. 3, p. 033501, 2011.
[20] I. G. Mikellides, R. R. Hofer, I. Katz, and D. M. Goebel, "The effectiveness of magnetic shielding in high-Isp Hall thrusters," in *Proc. 49th AIAA/ASME/SAE/ASEE Joint Propuls. Conf.*, San Jose, CA, USA, Jul. 2013.
[21] R. R. Hofer, B. A. Jorns, J. E. Polk, I. G. Mikellides, and J. S. Snyder, "Wear test of a magnetically shielded Hall thruster at 3000 seconds specific impulse," in *Proc. 33rd IEPC*, Washington, DC, USA, Oct. 2013.
[22] D. M. Goebel, R. R. Hofer, I. G. Mikellides, I. Katz, J. E. Polk, and B. Dotson, "Conducting wall Hall thrusters," in *Proc. 33rd IEPC*, Washington, DC, USA, Oct. 2013.
[23] H. Kamhawi *et al.*, "Design and performance evaluation of the NASA-300ms 20 kW Hall effect thruster," in *Proc. 33rd IEPC*, Washington, DC, USA, Oct. 2013.
[24] R. Conversano, D. Goebel, R. Hofer, T. Matlock, and R. Wirz, "Magnetically shielded miniature Hall thruster: Design and initial testing," in *Proc. 33rd IEPC*, Washington, DC, USA, Oct. 2013.
[25] A. I. Morozov, "Focusing of cold quasineutral beams in electromagnetic fields," *Soviet Phys. Doklady*, vol. 10, no. 8, pp. 775–777, 1966.
[26] A. I. Morozov, Y. V. Esipchuk, G. N. Tilinin, A. V. Trofimov, Y. A. Sharov, and G. Y. Shchepkin, "Plasma accelerator with closed electron drift and extended acceleration zone," *Soviet Phys. Techn. Phys.*, vol. 17, no. 1, pp. 38–45, 1972.
[27] A. I. Morozov and V. V. Savelyev, "Fundamentals of stationary plasma thruster theory," in *Reviews Plasma Physics*, vol. 21, B. B. Kadomtsev and V. D. Shafranov, Eds. New York, NY, USA: Kluwer Academic/Plenum Publishers, 2000.
[28] I. G. Mikellides, I. Katz, and R. R. Hofer, "Design of a laboratory Hall thruster with magnetically shielded channel walls, phase I: Numerical simulations," in *Proc. 47th AIAA/ASME/SAE/ASEE Joint Propuls. Conf.*, Atlanta, GA, USA, Jul. 2011.
[29] B. M. Ried, A. D. Gallimore, R. R. Hofer, Y. Li, and J. M. Haas, "Anode design and verification for a 6-kW Hall thruster," *JANNAF J. Propuls. Energetics*, vol. 3, no. 1, pp. 29–43, 2010.
[30] Y. Garnier, V. Veil, J. F. Roussel, and J. Bernard, "Low energy xenon ion sputtering of ceramics investigated for stationary plasma thrusters," *J. Vac. Sci. Technol. A*, vol. 17, no. 6, pp. 3246–3254, 1999.
[31] J. D. Sommerville and L. B. King, "Hall-effect thruster—Cathode coupling, Part I: Efficiency improvements from an extended outer pole," *J. Propuls. Power*, vol. 27, no. 4, pp. 744–753, 2011.
[32] J. D. Sommerville, "Hall-effect thruster-cathode coupling: The effect of cathode position and magnetic field topography," M.S. Thesis, Dept. Mech. Eng., Michigan Technol. Univ., Houghton, MI, USA, 2009.
[33] R. R. Hofer, J. M. Haas, and A. D. Gallimore, *Ion Voltage Diagnostics in the Far-Field Plume of a High-Specific Impulse Hall Thruster*. New York, NY, USA: BiblioGov, Jul. 2003.
[34] C. L. Enloe and J. R. Shell, "Optimizing the energy resolution of planar retarding potential analyzers," *Rev. Sci. Instrum.* vol. 63, no. 2, pp. 1788–1791, 1992.
[35] M. Tartz and H. Neumann, "Sputter yields of carbon materials under xenon ion incidence," *Plasma Process. Polymers*, vol. 4, no. S1, pp. 5633–5636, 2007.
[36] B. M. Ried, "The influence of neutral flow rate in the operation of Hall thrusters," M.S. thesis, Dept. Aerosp. Eng., Univ. Michigan, Ann Arbor, MI, USA, 2009.
[37] Y. Azziz, "Instrument development and plasma measurement on a 200-watt Hall thruster plume," M.S. thesis, Dept. Aeronautics Astronautics, Massachusetts Inst. Technol., Cambridge, MA, USA, 2003.
[38] T. E. Sheridan, "How big is a small Langmuir probe?" *Phys. Plasmas*, vol. 7, no. 7, pp. 3084–3088, 2000.
[39] J. M. Ekholm and W. A. Hargus, Jr., "E x B measurements of a 200 W xenon Hall thruster," in *Proc. 41st AIAA/ASME/SAE/ASEE Joint Propuls. Conf.*, Tucson, AZ, USA, Jul. 2005.

Ryan W. Conversano received the B.S. and M.S. degrees in aerospace engineering from the University of California at Los Angeles (UCLA), Los Angeles, CA, USA, in 2010 and 2011, respectively, where he is currently pursuing the Ph.D. degree in aerospace engineering.

He was involved in a variety of research disciplines, including high-power plasma-material interactions, lunar mission CubeSat mission studies, microsatellite mission design, biologically inspired flexible wing design, cylindrical ring-wing projectile analysis, and piezoelectric actuator testing, from 2008 to 2012. Since 2012, he has been involved in the Ph.D. research on the development and testing of the MaSMi Hall thruster. He has authored six technical publications, and is the lead inventor on a pending patent.

Mr. Conversano is currently a fellow of the NASA Space Technology Research Fellowship. He was a recipient of the NSF SEE-LA GK12 Fellowship in 2012, the AeroClub of Southern California Scholarship Award in 2011, and the UCLA Chancellor's Prize for Academic Excellence, the UCLA Graduate Student Research Mentorship, and the UCLA Graduate Division Student Support Award in 2010.

Dan M. Goebel (M'92–SM'96–F'99) received the B.S. degree in physics, the M.S. degree in electrical engineering, and the Ph.D. degree in applied plasma physics from the University of California at Los Angeles (UCLA), Los Angeles, CA, USA, in 1977, 1978, and 1981, respectively.

He is a Senior Research Scientist with the Jet Propulsion Laboratory (JPL), Pasadena, CA, USA, an Adjunct Professor of Electrical Engineering at the University of Southern California, Los Angeles, and an Adjunct Professor of Aerospace Engineering at UCLA. At JPL, he is responsible for the development of high-efficiency ion and Hall thrusters and advanced components, such as cathodes and grids. Previously, he was a Research Scientist at HRL Laboratories, Malibu, CA, USA, and a Principal Scientist at Hughes/Boeing EDD, Torrance, CA, USA, where he was the Supervisor of the Advanced Technology Group for microwave tube development and the Lead Scientist of the XIPS ion thruster program for commercial satellite station keeping. He has authored over 120 technical journal papers, 140 conference papers, one book entitled *Fundamentals of Electric Propulsion: Ion and Hall Thrusters* (2008), and holds 41 patents.

Dr. Goebel is a fellow of the American Institute of Aeronautics and Astronautics (AIAA) and the American Physical Society, and the former Chair of the IEEE EDS Technical Committee on Vacuum Devices and the AIAA Technical Committee on Electric Propulsion.

Richard R. Hofer received the B.S.E. degree in mechanical engineering and the B.S.E., M.S.E, and Ph.D. degrees in aerospace engineering from the University of Michigan, Ann Arbor, MI, USA, in 1998, 1998, 2000, and 2004, respectively.

He has been involved in research aimed at radically extending the performance and life of Hall thrusters, since joining the Jet Propulsion Laboratory (JPL), Pasadena, CA, USA, in 2005, where he leads activities to qualify Hall thrusters for use on NASA missions. He is a Senior Engineer at JPL, where he is the Technology Lead responsible for the development and qualification of Hall thrusters for deep space missions. He has authored over 80 technical publications in the field of electric propulsion, and holds three patents with one patent pending.

Dr. Hofer is an Associate Fellow of the American Institute of Aeronautics and Astronautics, and a member of the American Institute of Aeronautics and Astronautics Electric Propulsion Technical Committee. He was a recipient of the NASA Exceptional Achievement Medal and the JPL Lew Allen Award for Excellence in 2011.

Taylor S. Matlock received the B.S. degree in aerospace engineering from the Virginia Polytechnic Institute and State University, Blacksburg, VA, USA, in 2006, and the M.S. and Ph.D. degrees in aeronautics and astronautics from the Massachusetts Institute of Technology, Cambridge, MA, USA, in 2009 and 2012, respectively.

He was a Laboratory Engineer with the Electric Propulsion Laboratory, Air Force Research Laboratory, Edwards AFB, CA, USA, from 2006 to 2007, where he was involved in nonintrusive diagnostics for Hall thrusters. Since 2012, he has been a Post-Doctoral Researcher with the Department of Mechanical and Aerospace Engineering, University of California at Los Angeles, Los Angeles, CA, USA. His current research interests include plasma-material interactions, low-temperature plasma physics and diagnostics, and nonlinear plasma instabilities.

Dr. Matlock is a member of the American Institute of Aeronautics and Astronautics and the American Physical Society.

Richard E. Wirz received the B.S. degree in aerospace engineering and the B.S. degree in ocean engineering from the Virginia Polytechnic Institute and State University, Blacksburg, VA, USA, in 1992 and 1993, respectively, and the M.S. and Ph.D. degrees in aeronautics and applied sciences from the California Institute of Technology, Pasadena, CA, USA, in 2001 and 2005, respectively.

He was a Senior Engineer with the Electric Propulsion Group, Jet Propulsion Laboratory, Pasadena, from 2005 to 2009, where he was involved in modeling, experimental testing, and mission integration of electric thrusters. Since 2008, he has been an Assistant Professor with the Department of Mechanical and Aerospace Engineering, University of California at Los Angeles, Los Angeles, CA, USA. He designed and developed the world's first noble gas miniature ion thruster, and is a recognized expert in miniature and precision plasma thruster design and development, plasma modeling for electric thrusters, and advanced propulsion concepts. His current research interests include electric and micropropulsion, low-temperature plasma and plasma discharges, plasma-material interactions, spacecraft and space mission design, and alternative energy generation and storage.